Plasmonic Properties of Film over Nanowell Surfaces Fabricated by Nanosphere Lithography

Erin M. Hicks,[†] Xiaoyu Zhang,[†] Shengli Zou,[†] Olga Lyandres,[‡] Kenneth G. Spears,[†] George C. Schatz,[†] and Richard P. Van Duyne*[,†]

Department of Chemistry and Department of Biomedical Engineering, Northwestern University, 2145 Sheridan Road, Evanston, Illinois 60208-3113

Received: August 12, 2005; In Final Form: September 22, 2005

In this work, a detailed and systematic study of the plasmonic properties of a novel film over nanowell surface is investigated. These nanostructures are fabricated using nanosphere lithography and reactive ion etching and structurally characterized by AFM and SEM. The resulting structures show remarkably narrow plasmon bands in reflectance spectra (as little as 0.10 eV) and greater sensitivity to external dielectric environment than has been seen in other nanoparticle systems, resulting in an improvement in the figure of merit (FOM = refractive index sensitivity (eV·RIU^{-1})/full width at half-maximum (eV)) for refractive index sensing. Theoretical modeling for the plasmon spectra of these nanostructures is done using discrete dipole approximation code under periodic boundary conditions. The modeling results match the measurements accurately in aspects of the variation of the plasmon line shape with altering internanowell distance and dielectric environment.

Introduction

The unique size-dependent properties of nanometer-scale particles and templated surfaces have received significant attention in various fields, such as microelectronics[1,2] and medicine.[3,4] The optical properties, especially the plasmonic properties of noble metal nanostructures, are of particular interest since they exhibit selective photon absorption and scattering that are strongly dependent on their surface morphology. These plasmonic properties are used in a variety of applications including chemical and biological sensors,[5−8] surface-enhanced spectroscopies,[9,10] and near-field microscopy.[11]

Surface plasmons exist in two forms, propagating and localized. On a flat smooth film, the surface plasmon polaritons (SPPs) are propagating evanescent electromagnetic waves at the metal−dielectric interface, and are the result of collective oscillations of the conduction electrons in the metal. Localized surface plasmon resonances (LSPRs) are not propagating electromagnetic waves; rather they are localized electromagnetic fields near the surface of the isolated nanoparticles. It is possible to have both SPPs and LSPRs excited in some periodic,[12,13] colloidal,[14−16] or other nanosystems.[17] The unique interactions between the SPPs and LSPRs cause different enhancements of the electromagnetic fields and lead to new phenomena not observed in either extended or single particle systems.

The plasmon excitation can be monitored using either UV−visible extinction spectroscopy[17] or dark field resonant Rayleigh light scattering spectroscopy.[18] It has been well established that the wavelength of maximum extinction or scattering (λ_{max}) associated with the LSPR excitation is strongly and systematically dependent upon the composition, size, shape, and interparticle spacing of nanoparticles.[19−22] When surfaces are not optically transparent, the wavelength associated with minimum reflectivity (λ_{min}) provides an alternative measurement to locate the plasmon resonance.[23]

Although single nanoparticles and nanoparticle arrays have been extensively studied,[5,7,18,19,22] nanohole arrays have just begun to be analyzed as a new plasmonic construct since the discovery of enhanced transmission through subwavelength apertures.[24] Nanohole arrays exhibit characteristic transmission spectra[24−29] that are sensitive to the polarization of the light,[29] the shape of the hole,[27,29] the hole size,[30] the hole depth,[27] and the external dielectric environment.[6,30,31] To understand the mechanism of enhanced transmission that is observed from these nanostructures, a systematic study has been performed to look at the transition from nanoparticles to nanohole arrays.[32] From this work, the mechanism behind enhanced hole transmission is thought to be dominated by SPP excitation with nonnegligible contributions from LSPR excitation at the hole edges.[32,33] Although these arrays are different, physically and optically, from nanoparticles or smooth thin film that supports SPPs, they have also shown potential as biosensors[6,30] and surfaces for surface-enhanced Raman scattering.[9]

Uniformity in the interhole distance and the geometry of the nanoholes is critical to the elimination of variations in the electromagnetic coupling between holes. It is therefore crucial to identify a fabrication method that provides the precision and accuracy required to prevent noncoherent coupling. The methods heretofore used to create nanohole arrays are focused ion beam (FIB) milling,[24] electron beam lithography,[34] photolithography,[35] and colloidal lithography.[30,36,37] This paper describes the use of nanosphere lithography (NSL)[38] combined with reactive ion etching (RIE)[37] to fabricate well-ordered nanowell structures (Figure 1). NSL is a low-cost, parallel, surface-independent technique used for producing well-ordered array structures with nanometer precision.[12,38] NSL is based on the self-assembly of polystyrene or silica nanospheres into hexagonally close-packed monolayer and multilayer structures. These structures are then

* Corresponding author. Telephone: (847) 491-3516. Fax: (847) 491-7713. E-mail: vanduyne@chem.northwestern.edu.
[†] Department of Chemistry.
[‡] Department of Biomedical Engineering.

10.1021/jp0545400 CCC: $30.25
Published on Web 11/02/2005

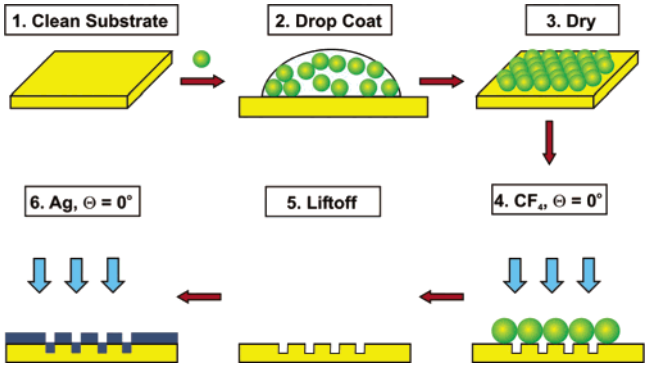

Figure 1. Schematic illustration of preparation of the film over nanowell surfaces.

used as lithographic masks for etching or deposition, creating an array of triangular nanowells or nanoparticles. The size and interhole spacing of nanowells can be tuned by using different sphere sizes, metal thickness, and etch times.

Herein, we systematically study the plasmonic properties of nanowell structures that have a thin silver overlayer. The effects of internanowell distance, mass thickness, nanowell depth, and the external dielectric environment have been studied in detail. Structures have been identified that have both extremely narrow plasmon resonances and very strong wavelength sensitivity to external dielectric constant. Theoretical modeling of the film over nanowell structure has been done using a two-dimensional array as a model system and the discrete dipole approximation. The calculated spectra are in good agreement with experiment, and we have used the results to interpret the dependence of the results on the architecture of these nanostructures.

Experimental Section

1. Materials. Absolute ethanol was purchased from Pharmco (Brookfield, CT). Methanol, acetone, methylene chloride, and pyridine were purchased from Fisher Scientific (Pittsburgh, PA). Ag pellets (99.99%, 0.125 in diameter) were obtained from Kurt J. Lesker (Pittsburgh, PA). Borosilicate glass surfaces, No. 2 Fisherbrand 18-mm circle coverslips, were purchased from Fisher Scientific (Pittsburgh, PA). n-doped silicon(111) was purchased from Wacker Siltronic (Portland, OR) and cut into $\sim 10-15$ mm^2 pieces. Polystyrene nanospheres with diameters (D) of 450 ± 4.95, 510 ± 7.65, 590 ± 12.98, and 720 ± 15.12 nm were received as a suspension in water. The nanosphere solutions were purchased from Interfacial Dynamics Corporation (Portland, OR). Millipore cartridges (Marlborough, MA) were used to purify water to a resistivity of 18 MΩ cm^{-1}. All materials were used without further purification.

2. Surface Preparation. Glass and silicon surfaces were cleaned in a piranha solution (1:3 30% H_2O_2:H_2SO_4) at 80 °C for 30 min. (**CAUTION***: Piranha solution should be handled with great care.*) Once cooled, the glass surfaces were rinsed with copious amounts of water and then sonicated for 60 min in 5:1:1 H_2O:NH_4OH:30% H_2O_2. Last, the glass was rinsed repeatedly with water and was stored in water until used.

3. Nanowell Preparation. For these experiments, single-layer colloidal crystal nanosphere masks were prepared by drop coating the nanosphere solution onto glass surfaces (Figure 1). Once the nanosphere masks were assembled, the surfaces were placed in a reactive ion etcher (RIE2000, South Bay Technology, Inc., San Clemente, CA) and etched for times from 10−25 min with CF_4 gas. The spheres were removed by allowing the samples to sit in warm piranha solution overnight. The samples were rinsed with copious amounts of ethanol and dried in N_2 before being mounted in a electron beam deposition system (Axxis Thin Film Electron Beam Evaporator, Kurt J. Lesker, Pittsburgh, PA).

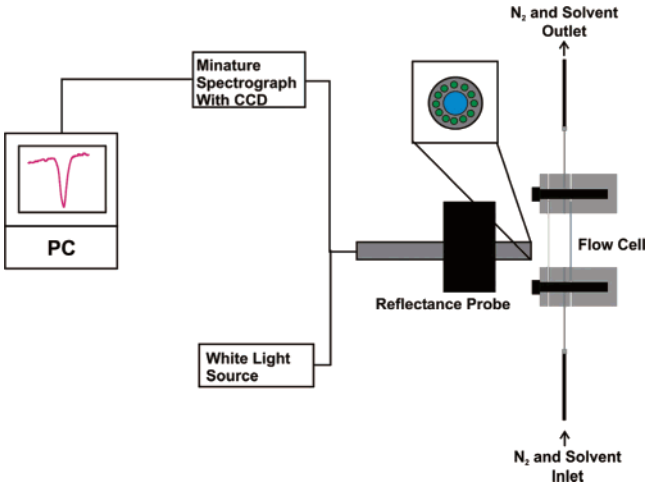

Figure 2. Scheme of apparatus used for LSPR spectroscopy in reflectance mode.

4. LSPR Reflectance Spectroscopy. Measurements were carried out using a SD2000 spectrometer coupled to a reflection probe (Ocean Optics, Dunedin, FL) and a halogen lamp (F-O-Lite H, World Precision Instruments, Sarasota, FL). The reflection probe consists of a tight bundle of 13 optical fibers (12 illumination fibers around a collection fiber) with a usable wavelength range of 400−900 nm (Figure 2). All reflectance spectra were collected against a mirror-like Ag film over glass surface as a reference.

5. Solvent Study. The experiment was done by drying the film over nanowells with nitrogen and recording an initial spectrum, filling the cell with a solvent and recording the resultant spectrum, and then purging the cell with nitrogen to restore the original spectrum before repeating the process with another solvent. Ethanol, methanol, acetone, methylene chloride, and pyridine were flowed over the sample to change the refractive index (RI) of the surrounding medium. Additionally, the sample was rinsed in methanol after methylene chloride. All the solvent shifts were completely reversible, with the exception of pyridine.[19]

6. Atomic Force Microscopy (AFM) and Scanning Tunneling Microscopy (STM). AFM images were collected on a Digital Instruments Nanoscope IV microscope and Nanoscope IIIa controller operating in tapping mode, using etched Si nanoprobe tips (TESP, Digital Instruments, Santa Barbara, CA). These tips had resonance frequencies between 280 and 320 kHz and were conical in shape with a cone angle of 20° and an effective radius of curvature at the tip of 10 nm. STM images of the film over nanowell surface were collected with a Molecular Imaging PicoPlus SPM in constant-current mode. The rendered image represents the smoothed topographic data.[48] Pt/Ir 80/20 mechanically cut tips were scanned at 1050 nm/s and a set point of 10 pA.

7. Scanning Electron Microscopy (SEM). SEM images were obtained using a Hitachi S-4500 microscope. An accelerating voltage of 5 kV was used for all SEM images.

Results and Discussion

1. Structural Characterization by AFM and SEM. Structural characterization of the samples prior to the optical measurements was conducted using both AFM and SEM. Figure 3 displays AFM images of three surfaces fabricated with

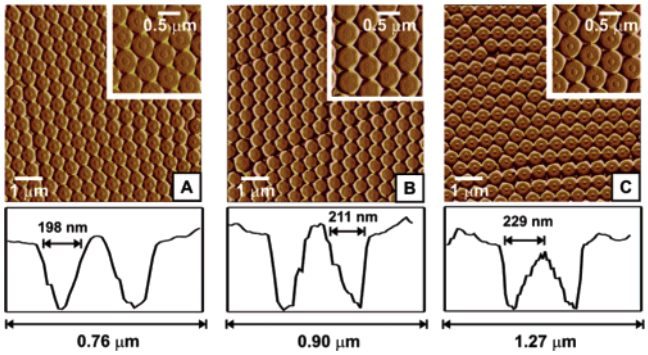

Figure 3. Tapping-mode AFM images of three etched glass substrates with different nanowell depths. (A) AFM image of the surface fabricated using a 10 min etching in CF_4. The average nanowell width is 197.6 ± 17.3 nm and depth is 30.3 ± 2.8 nm. (B) AFM image of the surface fabricated using a 19 min etching in CF_4. The average nanowell width is 211.7 ± 22.2 nm and depth is 57.6 ± 3.2 nm. (C) AFM image of the surface fabricated using a 25 min etching in CF_4. The average nanowell width is 229.1 ± 28.8 nm and depth is 65.2 ± 2.9 nm.

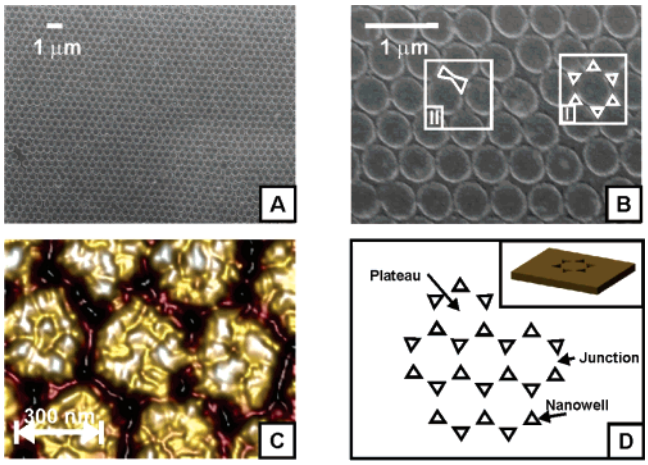

Figure 4. SEM images of Ag film over nanowell surface (D= 510 nm, d_m = 50 nm, and t_e = 10 min). (A) Well-packed area of over 40 μm^2; (B) magnified image of the same sample. The SEM accelerating voltage was 5 kV. (C) STM image of the surface. (D) Top-down schematic of the nanowell array. The inset is a three-dimensional rendering of the nanowell surface.

different etch times (t_e). Figure 3A is a 10 min etch, Figure 3B is a 19 min etch, and Figure 3C is a 25 min etch, with the corresponding line scans shown below each image. As the etch time increases, both the depth and in-plane width of the nanowells increase (Figure 3). The nanowell width increases from 198 nm in the 10 min etch to 229 nm in the 25 min etch due to under-etching of the polystyrene nanospheres used as a mask. The under-etching of the nanospheres is also evident in the smaller pedestal present in the center of the larger pedestals of the AFM images for all three etch times. The depths also increase with longer etching times, from 30 nm in the 10 min etch to 57 nm in the 19 min etch to 65 nm in the 25 min etch. All of these AFM images were taken of nanowell surfaces with no Ag deposited on them.

Ag films were then deposited onto the nanowell surfaces by electron beam deposition. The mass thickness of Ag film (d_m) was selected to be at least 50 nm to allow for efficient reflectance from the surface. Figure 4 details the substrate construction. Figure 4A,B shows the SEM images of the film over nanowell surfaces fabricated from a 10 min etch and a deposition of 50 nm of Ag. Figure 4A shows the large well-packed areas that can be achieved using NSL, on the order of 40 μm^2. Figure 4B is an enlargement of Figure 4A, and shows greater morphological details of the surface. There are two regions that can be seen in Figure 4B: region I is an area where there is good packing which produces discrete nanowells. In region II, there is a defect that affects the surrounding packing producing connected nanowells. The ratio of region I to region II depends on the etch time used to fabricate the surface. To further clarify the structure of the surface, Figure 4C,D shows both an image and a schematic with more highly magnified views of the surface. Figure 4C is a scanning tunneling microscope image of the surface showing that, in region I areas, most of the nanowells are discrete for this particular substrate. Figure 4D is a schematic of a region I surface. The inset is a three-dimensional rendering of the top-down view depicted in the larger scale.

2. Plasmonic Properties of Film over Nanowell Surfaces. Optical characterization, by systematic variation of several structural and environmental parameters, was conducted after structural characterization of the nanoscale morphology. Specifically, the plasmonic properties of the film over nanowells were explored by varying (1) the internanowell distance, (2) the mass thickness of the Ag overlayer, (3) the nanowell depth, and (4) the refractive index of the external environment.

2.1. Dependence on the Internanowell Distance. The control over the internanowell distance was achieved by varying the diameter of nanospheres, D, used as the etch mask. With an increase in D, a systematic shift of λ_{min} to longer wavelengths and a decrease in the full width at half-maximum (fwhm) of the plasmon peaks is observed in the reflectance spectra (Figure 5A). The increase in D concomitantly increases in the nanowell width. Specifically, the LSPR reflectance peak positions (λ_{min}) are 459, 487, 566, and 676 nm and the fwhm's are 0.17, 0.20, 0.13, and 0.11 eV for D = 450, 510, 590, and 720 nm, respectively.

Figure 5B plots the reflectance peak position, λ_{min}, for each film over nanowell surface as a function of D in nanometers, indicating a linear relationship with a slope close to unity (λ_{min} = 0.959D). The data points in Figure 5B are the averages taken over several surfaces (3−12 surfaces). The error bars represent standard deviations, which are between 1 and 5 nm, demonstrating the high reproducibility of both the surface fabrication and the plasmon measurements. This result provides important clues concerning the nature of the coupling mechanism that is responsible for the narrow plasmons (as little as 0.1 eV fwhm). In earlier work on one- and two-dimensional nanoparticle arrays, electrodynamic calculations and analytical theories were exploited to predict that sharp plasmonic/photonic line shapes should occur for particle arrays in a vacuum (refractive index (RI) = 1.0) when interparticle distances are equal to the plasmon peak position (λ_{max} = interparticle distance).[39,40] When the array is embedded in a medium, this diffractive coupling effect should generalize to λ_{max} = RI × interparticle distance, which has been proven by experiments. Our previous work has demonstrated λ_{max} = 1.5 × interparticle distance for linear arrays of Ag cylindrical nanoparticles on a glass surface and immersed in index-matched oil (for which RI = 1.5).[41]

In the present case, we do not have an index-matched structure, so it is possible that the coupling could occur through air or through glass. However, the observed slope of the linear fit in Figure 5B is 0.959, indicating that the coupling through air (RI = 1.0) is dominant.

2.2. Dependence on the Mass Thickness of Ag Film. Figure 6A shows the plasmon spectra of the Ag film over nanowell surfaces with fixed internanowell distance and nanowell depth (D = 510 nm, depth = 30 nm) and various mass thicknesses.

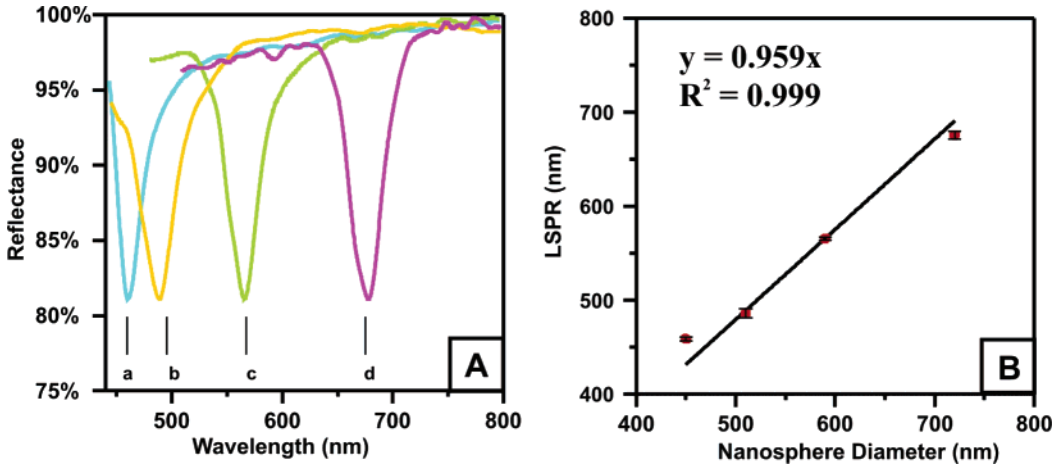

Figure 5. (A) Reflectance spectra of a series of film over nanowell samples with different polystyrene nanosphere diameters: (a) 450, (b) 510, (c) 590, and (d) 720 nm. For all samples, $t_e = 10$ min and $d_m = 50$ nm. (B) A linear relationship is seen between sphere size and peak position. Linear regression was used to fit data to the line described by the equation $\lambda_{min} = 0.959D$ ($R^2 = 0.999$). Each data point represents the average value recorded from at least three surfaces. Error bars show the standard deviations.

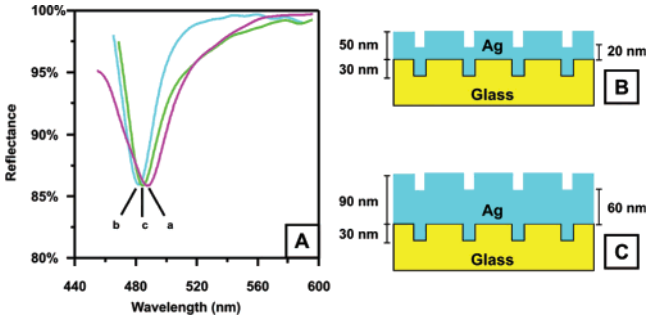

Figure 6. (A) Reflectance spectra of nanowell surfaces ($D = 510$ nm) with different silver film thicknesses. (a) $d_m = 50$ nm, (b) $d_m = 70$ nm, and (c) $d_m = 90$ nm. (B) and (C) are schematic side views of the substrates, drawn to scale, with $d_m = 50$ and 90 nm, respectively.

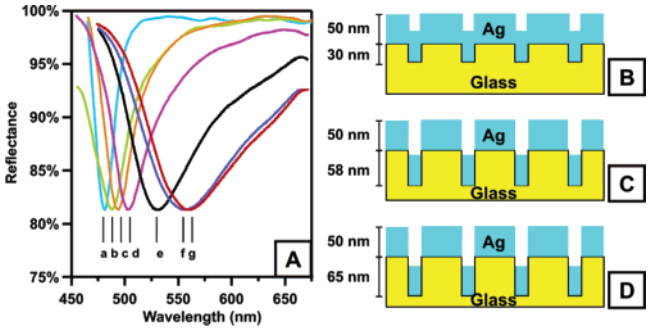

Figure 7. (A) Collection of reflectance spectra using a series of surfaces with various nanowell depths but fixed internanowell distance and mass thickness ($D = 510$ nm, $d_m = 50$ nm). (a) $t_e = 7$ min, (b) $t_e = 10$ min, (c) $t_e = 13$ min, (d) $t_e = 16$ min, (e) $t_e = 19$ min, (f) $t_e = 22$ min, and (g) $t_e = 25$ min. (B), (C), and (D) are schematic side views, drawn to scale, of the surfaces corresponding to the spectra b, e, and g in (A), respectively.

As the mass thickness increases from 50 to 70 to 90 nm, no dramatic changes in peak positions or fwhm's are observed. Schematic cross sections of the nanostructures are shown in Figure 6B,C. The metal film over nanowells can be mainly divided into two portions: (1) the top, i.e., metal film with nanoholes with a depth of 30 nm, and (2) the bottom, i.e., metal nanoparticles embedded in glass. When the Ag film is thick enough, e.g., 90 nm, the penetration depth of the light is not sufficient for wavelengths longer than 450 nm to reach into the bottom portion. Consequently, the nanoparticles embedded in the glass substrate have no significant contributions to the plasmonic spectra; rather, it is only the top portions of the metal film over nanowell surfaces that participate.

2.3. Dependence on the Nanowell Depth. Figure 7A displays a set of reflectance spectra from a series of surfaces with various nanowell depths but fixed internanowell distance and mass thickness ($D = 510$ nm, $d_m = 50$ nm). In Figure 7A, as the nanowell depth increases, the peak systematically shifts to longer wavelength and becomes broader. The structural and optical parameters are summarized in Table 1. In these experiments, the Ag film was chosen to have $d_m = 50$ nm so that the underlying glass surface, with RI = 1.52, would play a role in the plasmon spectra. As the nanowell deepens, the fraction of exposed glass increases (as depicted in Figure 7B−D). With more glass exposed, the plasmon peak position shifts to longer wavelengths. This is also in agreement with previous studies on the substrate effect on LSPR of Ag nanoparticles.[42]

With regard to the changes in the plasmon peak width, the coupling mechanism must be considered. When more glass is exposed, besides the through-air coupling, there is a greater amount of through-glass coupling. The averaging of the through air and through glass coupling mechanisms leads to the observed broadening of the plasmon bands. It is worth noting that a uniform refractive index is a critical factor to achieve the narrow plasmons, reported previously for nanoparticle arrays in both theory[39,40,43] and experiment.[41] In addition, minor shape changes in the nanowell structure, such as the increased in-plane width of nanowells caused by longer etching time (Figure 3), can affect the shape and location of the spectral peak.

2.4. Dependence on the External Dielectric Environment. After examining the dependence of the plasmon spectra on the structural parameters of the film over nanowell surfaces, we systematically explored the effect of external dielectric media on the plasmon peak by altering the surrounding solvent. For all of the surfaces used in this study, the metal thickness ($d_m = 50$ nm) and etch time ($t_e = 10$ min, nanowell depth = 30 nm) remained constant, while the sphere diameter was varied ($D = 450$, 510, and 590 nm). These sizes of nanospheres were selected so that the plasmon spectra were located within the 400−950 nm operating range of our UV−vis spectrometer. Figure 8A shows the reflectance spectra from the surface with $D = 590$ nm that was immersed in various refractive index media. The spectra for the samples with $D = 450$ and 510 nm are not shown, since they demonstrate trends similar to those in Figure 8A.

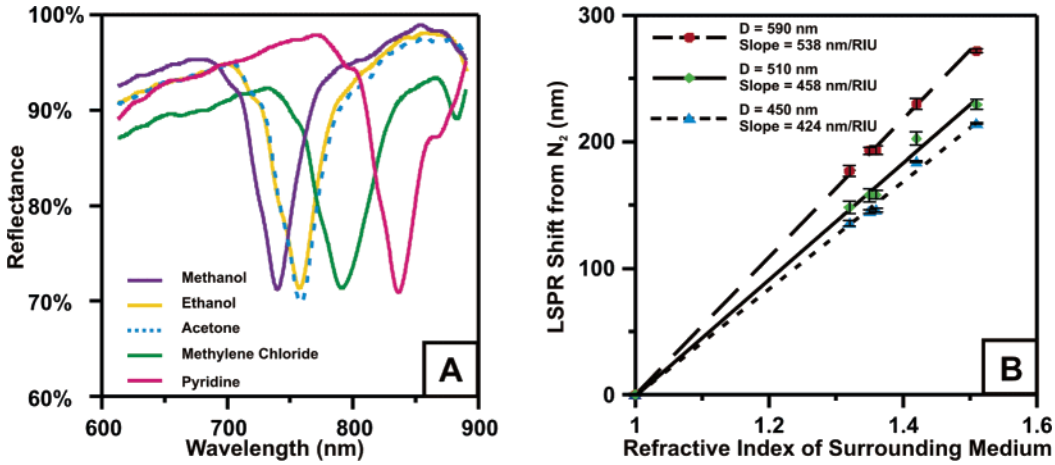

Figure 8. (A) Collection of reflectance spectra of Ag film over nanowell surface in different solvents ($D = 590$ nm, $d_m = 50$ nm). (B) Plots of λ_{min}(solvent) − λ_{min}(dry nitrogen) versus refractive index of the solvent for three nanosphere sizes: $D = 450$, 510, and 590 nm. Each data point represents the average value obtained from at least three surfaces. Error bars show the standard deviations. For all surface preparations, $d_m = 50$ nm and $t_e = 10$ min.

TABLE 1: Reflectance Data for Ag Film over Nanowells ($D = 510$ nm, $d_m = 50$ nm) on Glass with Various Etch Times

spectrum	RIE time (min)	depth (nm)	LSPR (nm)	fwhm (eV)
a	7	20	480	0.11
b	10	30	484	0.19
c	13	38	494	0.18
d	16	53	503	0.23
e	19	58	529	0.32
f	22	63	555	0.37
g	25	65	558	0.34

Figure 8B shows plots of [λ_{min}(solvent) − λ_{min}(dry nitrogen)] for each film over nanowell surface as a function of the refractive index of the surrounding medium. We have plotted the data as a function of peak position shift referenced to the dry nitrogen value in order to normalize the data and better compare the slopes for samples with different internanowell distances. Each data point in Figure 8B represents the average value obtained from at least three surfaces. Error bars show the standard deviations. Within this range of refractive index units, the data points for the surfaces fabricated using the same size polystyrene nanosphere can be fit well to a linear regression. We find that the film over nanowell surface using the largest sphere ($D = 590$ nm) is most sensitive to changes in the surrounding refractive index, followed by $D = 510$ nm and then $D = 450$ nm. For the most sensitive film over nanowell surfaces ($D = 590$ nm), the linear regression analysis yielded a refractive index sensitivity of 538 nm/refractive index unit (RIU), which means that every 0.002 change in the refractive index of the solvent will produce a change in the peak position of approximately 1 nm. To summarize the data above, since we found that $\lambda_{min} \approx$ (RI) × (nanosphere diameter), then $\Delta\lambda_{min} \approx$ (RI − 1) × (nanosphere diameter). This means that the RI sensitivity is just the nanosphere diameter, and the larger nanospheres will have the largest sensitivity. To place these results in context, it should be noted that the previously published sensitivity of both single gold nanoholes and nanohole arrays to refractive index is 100−400 nm/RIU.[6,30] In addition, the sensitivity of NSL fabricated Ag nanoparticles is 191−230 nm/RIU[18,19] and that of gold nanoshells is 328.5 nm/RIU.[44]

Furthermore, the overall refractive index sensitivity also depends on the fwhm. A "figure of merit" (FOM) is defined in eq 1, to quantitatively evaluate the refractive index sensitivity of various sensing platforms.[45]

$$\text{FOM} = \frac{m\ (\text{eV RIU}^{-1})}{\text{fwhm (eV)}} \qquad (1)$$

where m is the linear regression slope for the refractive index dependence. The films over nanowell surfaces exhibit extremely narrow plasmon peaks with fwhm as little as 0.1 eV and exceedingly large linear regression slopes as steep as 538 nm/RIU, which result in a favorable FOM of 14.5.

3. Theoretical Discussion. Previous work by Zou et al.[39,40,43] has predicted narrowed plasmon peaks in extinction from one- and two-dimensional arrays of nanoparticles. The narrow peaks are caused by coherent dipolar (photonic) interactions between the particles when the incident wavelength of the light is close in value to the interparticle distance. The mechanism behind the present results is similar to this earlier work, although the theory needed to describe the nanohole structures is different, given that the present experiments refer to suppressed reflectance rather than enhanced extinction. Thus, for an array of nanoholes, the coherent interactions between nanoholes lead to stronger local electric fields around nanoholes; however, the transparency is enhanced instead of extinction.[25,27,46]

To model the experimental system, a periodic boundary condition version of the discrete dipole approximation (DDA) method[47] was used similar to that described previously by Zou and Schatz.[40] This method is a fully retarded finite element based computational approach that provides the flexibility for describing arbitrary film structures. We first modeled exactly the same structures as in the experiments, meaning that the thickness of the film is taken to be the same both in the nanoholes and on

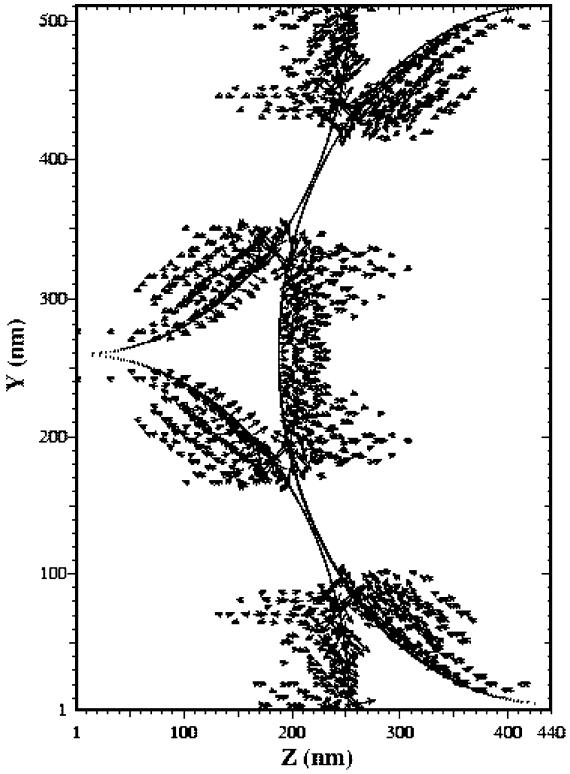

Figure 9. Induced polarization corresponding to a wavelength of 480 nm for 510 nm nanoparticles and *Z* polarization.

the plateau regions that are produced when the mask is removed. With reference to Figure 4, this means that the film is composed of flat cylindrical disks of a given thickness of metal on the plateau regions, and then nanowells with the same thickness. We find that, as the thickness of the metal in the nanowell is varied, the resonance wavelengths do not change significantly, which is consistent with our earlier conclusion that the reflection dips are determined by the region of the film at the top of the wells rather than the metal in the nanowells. Given this, we simplified the calculations by removing the metal in the wells, and the results that we present will all refer to a structure in which the only metal present is on the plateau regions. We also leave out the glass surface, as this was found to have minimal influence on the resonance wavelength (with exception of the work described in Figure 7).

To understand the nature of the plasmon excitation, a map of the induced dipole field was generated (Figure 9) for a wavelength corresponding to the reflection minimum (choosing $D = 510$ nm). In these calculations, the grid spacing in the DDA method is taken to be 5 nm. This large spacing may lead to 10 nm variations in the resonance wavelengths, but this is comparable to the experimental uncertainty and is thus of minor consequence. Figure 9 shows results for one unit cell, using polarization along the *Z* direction. Only the largest induced dipoles are included in the plot. The wave vector is always in the *X* direction, which is perpendicular to the surface.

The plane considered in Figure 9 is the top layer of the surface, which is where the polarization is largest (consistent with our earlier conclusions). The results show that the polarization is localized around the nanohole region, with the largest polarizations being associated with "junctions" where the nanoparticles almost touch. Regions where the nanoparticles do touch are "shorted out", and there is also little polarization in the centers of each plateau region. This means that it is best to think of the plasmon excitation as being "localized to the

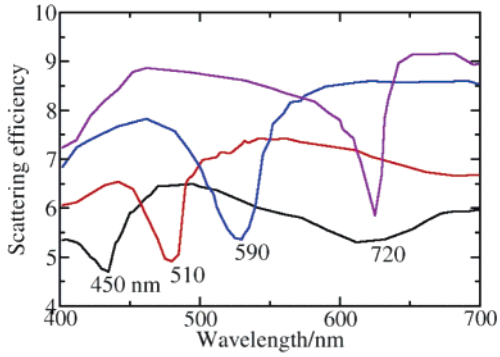

Figure 10. Theoretical calculations of scattering spectra of nanowell surfaces fabricated using different nanosphere sizes.

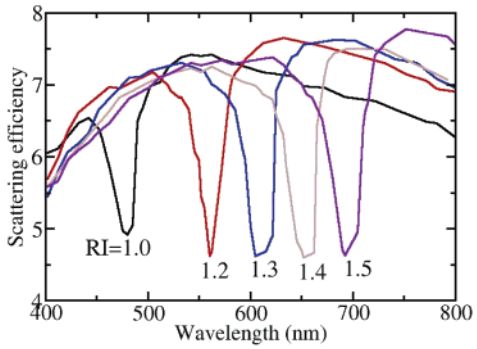

Figure 11. Theoretical calculations of scattering spectra of nanowell surfaces fabricated with 510 nm nanospheres surrounded by different media.

nanoholes", rather than "localized to nanoparticles", as was the case in our earlier studies of coupled nanoparticles. In addition, Figure 9 shows an example of what might be termed a "three particle junction", in which the polarization is large all around the triangular hole rather than just when pairs of particles nearly touch.

To further study the experiments, we have performed calculations in which the sphere diameter was varied for fixed film thickness. Figure 10 presents results for four choices of the diameter. This shows that when the diameter is 450 nm, a spectral dip at 424 nm wavelength is calculated; this theoretical λ_{min} is 8% away from the experimentally obtained λ_{min} of 459 nm. The calculated λ_{min} values for other nanosphere sizes (510, 590, and 720 nm) are found to be 480, 527, and 625 nm, respectively. All of these values are about 8% smaller than the experiments, which is probably a measure of the error in our idealized model of the film structure (i.e., leaving out the glass surface and metal in the nanowells). Also, in the model, all the polystyrene nanospheres are assumed to be in direct contact, while it is clear from Figure 4 that there is space between the nanospheres. Therefore, the calculated λ_{min} is smaller than that in the experimental measurements.

Another aspect of our modeling was concerned with the effect of varying the external dielectric constant. Here we take the diameter of the polystyrene nanospheres to be 510 nm, the metal thickness is taken to be 50 nm, and the nanowell depth is 50 nm. Figure 11 shows that the resonance wavelengths red shift when the index of refraction of the medium increases. In the calculations, the resonance wavelength is at 480 nm when the film is in a vacuum; it red shifts to 693 nm when the index of refraction is 1.5. In the experiment, the resonance wavelength is at 483 nm when the film is in a vacuum; it red shifts to 713 nm when the medium refractive index is changed to 1.51. The variation in resonance wavelength with index of refraction of

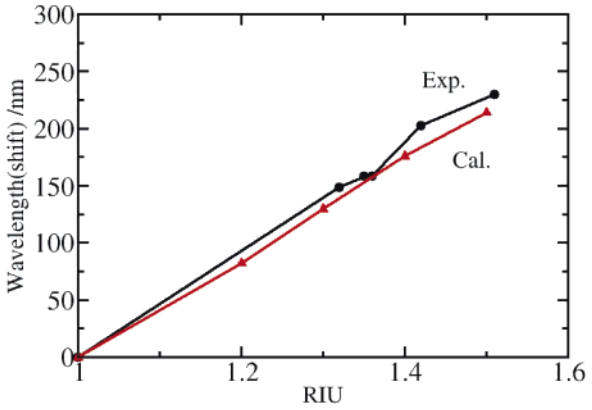

Figure 12. Comparison of shifts from theoretical calculations in a vacuum of resonance wavelengths and experimental results in N_2 for film over nanowell surfaces in different media vs indices of refraction of the media.

the medium is presented in Figure 12. This shows excellent agreement between theory and experiment. In the experiment, the slope of the straight line is 450 nm/RIU while the calculations give 426 nm/RIU (Figure 8). This slope grows linearly with increasing diameter of the polystyrene nanospheres, which is consistent with our earlier discussion that the slope is simply given by the diameter.

Conclusions

The results presented above show the unique plasmonic characteristics of film over nanowell surfaces. These nanostructures were fabricated using the combination of NSL and RIE, and then characterized by AFM, SEM, and LSPR reflectance spectroscopy. The Ag film over well-ordered, triangular cross-sectional nanowells exhibits narrow plasmon peaks, the position and shape of which can be tuned by varying the structural parameters during fabrication. By increasing the diameter of the nanosphere used as the etch mask, the plasmon peak shifts to longer wavelength. The relationship between the peak position and the nanosphere diameter has been solved as $\lambda_{min} = 0.959D$. As the nanowells deepen, a systematic red shift and peak broadening were observed due to the exposure of the underlying glass surface.

The plasmon peaks are not only controlled by the structural parameters, but are also extremely sensitive to the surrounding dielectric environment. As the refractive index of the surrounding medium increases, the plasmon peak shifts to longer wavelengths. There is a linear relationship between λ_{min} and the refractive index of the external dielectric medium. The sensitivity increases with larger nanosphere diameter. For example, the most sensitive surfaces among those evaluated were fabricated using polystyrene nanospheres with a diameter of 590 nm, which shows the linear regression slope as large as 538 nm/RIU, i.e., an approximately 1 nm shift in the plasmon peak with the change of 0.002 RIU in the refractive index.

The theoretical results modeled the system as a two-dimensional hexagonal array of touching circular disks, and we found that this model provided a semiquantitative description of the narrow resonance structures. Plots of the induced polarization show that the plasmon excitation is localized to the top portion of Ag films, and to regions around the three particle junction where the disks nearly touch. This means that the film over nanowell structure is best thought of as consisting of coupled nanoholes, rather than as coupled nanoparticles, although there is clearly a continuous transition between one limit and the other as the disk diameter is varied relative to the disk spacing. We also find that diffractive coupling between nanowells causes the plasmons to be remarkably narrow (~0.15 eV fwhm). Our experimental results showed that if the nanowell is deep enough compared to the metal film thickness, the disks can couple through glass as well as through air, therefore red shifting and broadening the peaks (~0.33 eV fwhm).

The experimental and theoretical results show the first example of a two-dimensional array that has been specifically fabricated to take advantage of diffractively coupled plasmon resonances. This has yielded array structures with narrow plasmon bands and greater sensitivity to external dielectric constant than has been seen in other nanostructures. Future studies will allow these surfaces to be used in a wide variety of applications, including developing novel refractive index based platforms and fabricating innovative nanostructured catalysts.

Acknowledgment. The authors thank David Andrews for taking the STM image presented in this paper. The authors also acknowledge Ms. Chanda R. Yonzon, Ms. Jing Zhao, Dr. Adam D. McFarland, and Dr. Douglas A. Stuart for helpful discussions. This research was supported by the National Science Foundation (DMR-0076097), Nanoscale Science and Engineering Initiative of the National Science Foundation under an NSF Award (EEC-0118025), CHE-0414554, and the Air Force Office of Scientific Research MURI program (F49620-02-1-0381).

References and Notes

(1) Liang, Y.; Zhai, L.; Zhao, X.; Xu, D. *J. Phys. Chem. B* **2005**, *109*, 7120.
(2) Choi, W. B.; Bae, E.; Kang, D.; Chae, S.; Cheong, B.; Ko, J.; Lee, E.; Park, W. *Nanotechnology* **2004**, *15*, S512.
(3) Haes, A. J.; Chang, L.; Klein, W. L.; Van Duyne, R. P. *J. Am. Chem. Soc.* **2005**, *127*, 2264.
(4) Li, Y. Y.; Cunin, F.; Link, J. R.; Gao, T.; Betts, R. E.; Reiver, S. H.; Chin, V.; Bhatia, S. N.; Sailor, M. J. *Science* **2003**, *299*, 2045.
(5) Haes, A. J.; Van Duyne, R. P. *J. Am. Chem. Soc.* **2002**, *124*, 10596.
(6) Brolo, A. G.; Gordon, R.; Leathem, B.; Kavanagh, K. L. *Langmuir* **2004**, *20*, 4813.
(7) Haes, A. J.; Zou, S.; Schatz, G. C.; Van Duyne, R. P. *J. Phys. Chem. B* **2004**, *108*, 109.
(8) Haes, A. J.; Zou, S.; Schatz, G. C.; Van Duyne, R. P. *J. Phys. Chem. B* **2004**, *108*, 6961.
(9) Brolo, A. G.; Arctander, E.; Gordon, R.; Leathem, B.; Kavanagh, K. L. *Nano Lett.* **2004**, *4*, 2015.
(10) Dick, L. A.; McFarland, A. D.; Haynes, C. L.; Van Duyne, R. P. *J. Phys. Chem. B* **2002**, *106*, 853.
(11) El-Sayed, M. A. *Acc. Chem. Res.* **2001**, *34*, 257.
(12) Hulteen, J. C.; Van Duyne, R. P. *J. Vac. Sci. Technol., A* **1995**, *13*, 1553.
(13) GarciaVidal, F. J.; Pendry, J. B. *Phys. Rev. Lett.* **1996**, *77*, 1163.
(14) Zhang, H.-L.; Evans, S. D.; Henderson, J. R.; Miles, R. E.; Shen, T.-H. *Nanotechology* **2002**, *13*, 439.
(15) Jana, N. R.; Gearheart, L.; Obare, S. O.; Murphy, C. J. *Langmuir* **2002**, *18*, 922.
(16) Gole, A.; Murphy, C. J. *Chem. Mater.* **2005**, *17*, 1325.
(17) Jensen, T. R.; Schatz, G. C.; Van Duyne, R. P. *J. Phys. Chem. B* **1999**, *103*, 2394.
(18) McFarland, A. D.; Van Duyne, R. P. *Nano Lett.* **2003**, *3*, 1057.
(19) Malinsky, M. D.; Kelly, K. L.; Schatz, G. C.; Van Duyne, R. P. *J. Am. Chem. Soc.* **2001**, *123*, 1471.
(20) Link, S.; El-Sayed, M. A. *J. Phys. Chem. B* **1999**, *103*, 8410.
(21) Kreibig, U., Vollmer, M. *Optical Properties of Metal Clusters*; Springer-Verlag: Heidelberg, Germany, 1995; Vol. 25, p 532.
(22) Jensen, T. R.; Duval, M. L.; Kelly, L.; Lazarides, A.; Schatz, G. C.; Van Duyne, R. P. *J. Phys. Chem. B* **1999**, *103*, 9846.
(23) Zhang, X.; Young, M. A.; Lyandres, O.; Van Duyne, R. P. *J. Am. Chem. Soc.* **2005**, *127*, 4484.
(24) Ebbesen, T. W.; Lezec, H. J.; Ghaemi, H. F.; Thio, T.; Wolff, P. A. *Nature* **1998**, *391*, 667.
(25) Barnes, W. L.; Dereux, A.; Ebbesen, T. W. *Nature* **2003**, *424*, 824.
(26) Barnes, W. L.; Murray, W. A.; Dintinger, J.; Devaux, E.; Ebbesen, T. W. *Phys. Rev. Lett.* **2004**, *92*, 107401.
(27) Degiron, A.; Lezec, H. J.; Barnes, W. L.; Ebbesen, T. W. *Appl. Phys. Lett.* **2002**, *81*, 4327.

(28) Yin, L.; Vlasko-Vlasov, V. K.; Rydh, A.; Pearson, J.; Welp, U.; Chang, S. H.; Gray, S. K.; Schatz, G. C.; Brown, D. B.; Kimball, C. W. *Appl. Phys. Lett.* **2004**, *85*, 467.

(29) Gordon, R.; Brolo, A. G.; McKinnon, A.; Rajora, A.; Leathem, B.; Kavanagh, K. L. *Phys. Rev. Lett.* **2004**, *92*, 037401.

(30) Prikulis, J.; Hanarp, P.; Olofsson, L.; Sutherland, D.; Kall, M. *Nano Lett.* **2004**, *4*, 1003.

(31) Kim, T. J.; Thio, T.; Ebbesen, T. W.; Grupp, D. E.; Lezec, H. J. *Opt. Lett.* **1999**, *24*, 256.

(32) Murray, W. A.; Astilean, S.; Barnes, W. L. *Phys. Rev. B* **2004**, *69*, 165407.

(33) Chang, S.-H.; Gray, S. K.; Schatz, G. C. *Opt. Express* **2005**, *13*, 3150.

(34) Awad, Y.; Lavallee, E.; Lau, K. M.; Beauvais, J.; Drouin, D.; Cloutier, M.; Turcotte, D.; Yang, P.; Kelkar, P. *J. Vac. Sci. Technol., A* **2004**, *22*, 1040.

(35) Grego, S.; Jarvis, T. W.; Stoner, B. S.; Lewis, J. S. *Langmuir* **2005**, *21*, 4971.

(36) Jiang, P.; McFarland, M. J. *J. Am. Chem. Soc.* **2005**, *127*, 3710.

(37) Whitney, A. V.; Myers, B. D.; Van Duyne, R. P. *Nano Lett.* **2004**, *4*, 1507.

(38) Haynes, C. L.; Van Duyne, R. P. *J. Phys. Chem. B* **2001**, *105*, 5599.

(39) Zou, S.; Janel, N.; Schatz, G. C. *J. Chem. Phys* **2004**, *120*, 10871.

(40) Zou, S.; Schatz, G. C. *Proc. SPIE-Int. Soc. Opt. Eng.* **2004**, *5513*, 22.

(41) Hicks, E. M.; Zou, S.; Gunnarsson, L.; Rindzevicius, T.; Spears, K. G.; Kasemo, B.; Kall, M.; Schatz, G. C.; Van Duyne, R. P. *Nano Lett.* **2005**, *5*, 1065.

(42) Malinsky, M. D.; Kelly, K. L.; Schatz, G. C.; Van Duyne, R. P. *J. Phys. Chem. B* **2001**, *105*, 2343.

(43) Zou, S.; Schatz, G. C. *J. Chem. Phys.* **2004**, *121*, 12606.

(44) Sun, Y. G.; Xia, Y. N. *Analyst* **2003**, *128*, 686.

(45) Sherry, L. J.; Chang, S.-H.; Wiley: B. J.; Xia, Y.; Schatz, G. C.; Van Duyne, R. P. *Nano Lett.* **2005**, *5*, 2034.

(46) Hubert, C.; Rumyantseva, A.; Lerondel, G.; Grand, J.; Kostcheev, S.; Billot, L.; Vial, A.; Bachelot, R.; Royer, P.; Chang, S. H.; Wiederrecht, G. P.; Schatz, G. C. *Nano Lett.* **2005**, *5*, 615.

(47) Draine, B. T.; Flatau, P. J. *User Guide for the Discrete Dipole Approximation Code DDSCAT.6.0*; 2003.

(48) Nonatec Electronics WZxM Freeware, http://www.nanotec.es.